MDPI

*Communication*

# In Situ Synchrotron HEXRD Study on the Deformation Mechanism of a Nickel-Based Superalloy during Medium-Temperature Compression

Hao Wang [1,*], Ruolan Tong [2], Huashan Shang [1], Aixue Sha [1], Guangxu Liu [1], Lin Song [2,*] and Tiebang Zhang [2]

1 Beijing Institute of Aeronautical Materials, AECC, Beijing 100095, China
2 State Key Laboratory of Solidification Processing, Northwestern Polytechnical University, Xi'an 710072, China
* Correspondence: whbiam@163.com (H.W.); songlin@nwpu.edu.cn (L.S.)

**Abstract:** The $\gamma'$ phase has an important influence on the deformation mechanism of solid-solution strengthening nickel-based superalloys. The microfracture behavior of the alloy depends on the mechanism of stress and strain partitioning between the $\gamma$ and $\gamma'$ phase under load. In this study, the in situ synchrotron radiation high-energy X-ray diffraction technique was used to observe the deformation process of the FGH96 nickel-based superalloy with a $\gamma'$ volume fraction of about 40% at 650 °C and 750 °C. The results show that the (111) reflection had the greatest stiffness and showed plastic deformation first; while the (200) reflection bore a larger load. The $\gamma$ phase yielded first and began to deform plastically; then the load was transferred to the $\gamma'$ phase. At 650 °C, the plastic deformation of the $\gamma'$ phase was relatively higher; while at 750 °C, the $\gamma'$ particle basically maintained elastic deformation with a tiny amount of plastic deformation.

**Keywords:** Ni-based superalloy; in situ HEXRD; deformation mechanism; load partitioning

## 1. Introduction

Nickel-based superalloys are widely used in aviation, aerospace and naval fields due to their excellent mechanical properties under complex loads and environments [1]. The microstructure of these alloys is composed of a $\gamma$ matrix embedded with $L1_2$-structured $\gamma'$ (Ni$_3$Al) strengthening particles and dispersed carbides [2]. As the main strengthening phase, the size and volume fraction of the $\gamma'$ phase have a vital effect on the mechanical properties. Under the application temperatures, the mechanical properties of the nickel-based superalloy are closely related to the coordinated deformation behavior between the $\gamma$ matrix and the $\gamma'$ phase, as well as the size, volume fraction, morphology and distribution of the $\gamma'$ [3–7]. The nickel-based superalloys with a high $\gamma'$ volume fraction and large particle size show an anomalous yield behavior: the yield strength first remains unchanged or decreases slightly with an increasing temperature, from room temperature to 600 °C, then increases abnormally from 600 °C to 750 °C and drops sharply above 750 °C [8,9]. This phenomenon is related to the Kear–Wilsdorf (K–W) dislocation locking; the flow stresses at peak temperatures are more than 2.5 times greater than that at room temperature. The dislocations cross-slip from the {111} plane to the {001} plane, which has a low-energy antiphase domain boundary, forming sessile dislocations [10,11]. However, the yield strength of nickel-based superalloys with a low $\gamma'$ volume fraction and a small particle size remains unchanged or monotonically decreases with an increasing temperature [12], which may be related to the instability of the $\gamma'$ phase, the lack of cross-slip and other strengthening mechanisms.

In situ neutron diffraction and X-ray diffraction are effective methods for studying the deformation behavior of nickel-based superalloys, especially on the load partitioning behavior of the $\gamma/\gamma'$ phase. Jaladurgam et al. [13] studied the phase transformation and mechanical response in a precipitation-hardening nickel-based alloy with different particle

sizes under tensile conditions at low temperatures (20, 100 and 300 K), and proved that the particle size and temperature have an effect on the intergranular and intragranular load transfer. The load in fine-grained superalloys moved from <220> to <200>. The <100> orientated $\gamma'$ phase, which is coherent with the matrix, accumulated large lattice strain, and the two phases demonstrated a coordinated deformation. For the coarse-grained material, <220> yielded first, and the load was transferred to <200> and the $\gamma'$ phase. The amount of load partitioning increased with the decrease in temperature. Jaladurgam et al. [14] also studied the influence of particle size on the deformation mechanism and load partitioning in a low $\gamma'$ volume fraction alloy at room temperature. The fine $\gamma'$ particles and matrix generated shear deformations together without load redistribution. The coarse $\gamma'$ particles were surrounded by an Orowan loop and the load was transferred from the matrix to the $\gamma'$ particles. The alloy with a high $\gamma'$ phase volume fraction initially underwent shear co-deformation, and then the critical stress of the Orowan loop was increased due to the small particle spacing, resulting in the increase in the work hardening rate and the load partitioning under high stress. Grant et al. [15] found that at the early stage of plastic deformation, the $\gamma'$ phase was sheared by dislocations regardless of the $\gamma'$ particle size. In further deformations, the load transfer in the Orowan loop occurred in the medium-size and coarse $\gamma'$ particles, while this phenomenon did not occur in the fine $\gamma'$ particles, where only shear deformations occurred. Francis et al. [16] conducted in situ compression neutron diffraction experiments at 750 °C on the RR750 polycrystalline nickel-based superalloy and established a two-site elasto-plastic self-consistent (EPSC) model to study the influence of the $\gamma'$ phase size on the deformation mechanism. The results showed that the fine $\gamma'$ particles and the $\gamma$ phase deformed together. However, there was a load transfer between coarse $\gamma'$ particles and the $\gamma$ phase. The stacking faults were confined to the $\gamma$ phase, and the matrix dislocation could not pass through the $\gamma'$ phase. The above studies show that the load transfer mechanism of the alloy varies with the volume fraction and size of the $\gamma'$ phase.

In this study, compression tests on FGH96 alloys with an average grain size of approximately 30 μm and a $\gamma'$ volume fraction of 40% were conducted at 650 °C and 750 °C, which were close to the service temperature. The changes in the diffraction peaks during the compression process were recorded by an in situ synchrotron radiation XRD technique, and the defects were analyzed by transmission electron microscopy. The deformation mechanism of the nickel-based FGH96 superalloy at medium temperatures was discussed.

## 2. Experiments

The FGH96 superalloy billet was prepared using the powder metallurgy method. The chemical composition (wt. %) of the FGH96 superalloy ingot: 12.9% Co, 15.7% Cr, 4% Mo, 4% W, 2.1% Al, 3.7% Ti, 0.7% Nb, 0.05% C, 0.03% B, 0.05% Zr and balanced Ni. The FGH96 alloy powders (<270 mesh) were fabricated using argon atomization technology. The melt flow rate was 3.5~4 kg/min. The cooling rate was $10^5$~$10^6$ K/s and the powder size distribution was within the range of 50~150 μm. Chemical analysis has shown that the oxygen content in the powder was less than 0.01 wt.%. The powders were consolidated using hot isostatic pressing (HIP) at 1170 °C/140 MPa/5 h. Then, the HIPed ingot was hot extruded and isothermal forged below the solvus temperature. After forging, the pancake was heat treated at 1160 °C for 4 h for the solid solution and then aged at 760 °C for 16 h, followed by air cooling. Cylinders with a diameter of 4 mm and a height of 8 mm were machined from the ingot. Compression tests were conducted at the strain rate of $10^{-3}$ s$^{-1}$ until fracture at 650 °C and 750 °C. Taking the Poisson effect into account, the cross-sectional area and the length of the sample change over time during deformation. In order to evaluate the deformation more accurately, the loads and displacements in the engineering test were converted into true stresses (dividing the length of the specimen by the volume of the specimen, and then multiplying by the stress) and strains (the logarithm of the ratio of the actual length to the initial length of the sample). The strain-hardening rate, i.e., the variation rate of the true stress in respect to the true strain, was obtained

by deriving the true stress–true strain curve, which reflects the work hardening under different strain conditions. In situ high-energy X-ray diffraction (HEXRD) measurements were conducted in the Deutsches Elektronen-Synchrotron (DESY) in Hamburg, utilizing the P07EH3 beamline at Helmholtz-Zentrum Geesthacht at PETRA III on the DIL 805 A/D compression machine, with a beam size of $0.4 \times 0.4$ mm$^2$ and a wavelength of 0.124 Å. The diffraction images were recorded on the two-dimensional detector. Debye–Scherrer diffraction rings were unrolled by the FIT2D software and integrated along the loading direction (LD) and traversing direction (TD), within a range of $\pm 10°$, into a series of one-dimensional XRD patterns. The lattice strain $\varepsilon_{hkl}$ was calculated as:

$$\varepsilon_{hkl} = \left( d^1_{hkl} - d^0_{hkl} \right) / d^0_{hkl} \tag{1}$$

where $d^0_{hkl}$ and $d^1_{hkl}$ are the interplanar spacing $d$ of the {$hkl$} lattice planes in the conditions of the initial stress-free state and the loading state, respectively. The high exponential $\gamma'$ phase reflection can be determined by referring to the low exponential $\gamma'$ phase superlattice diffraction. Information about the single phase and peak splitting was obtained by deconvolution fitting, in accordance with the pseudo-Vogit function.

## 3. Results and Discussion

The compression curves of the FGH96 alloy at different temperatures are shown in Figure 1. The yield strength at 750 °C and 650 °C of the FGH96 alloy was 640 MPa and 720 MPa, respectively. Limited by the highest stress of the DIL 805 A/D machine, the ultimate compressive strength and maximum true strain were 1448 MPa and 7.3%, and 1406 MPa and 9.9%, respectively. The work hardening rate of the FGH96 alloy at 650 °C was significantly higher than that at 750 °C, indicating a higher amount of dislocation actuation. This study is different from the phenomenon described in the literature [17], because the FGH96 alloy has a higher volume fraction (nearly 40%) of the $\gamma'$ phase. In general, the stress decreased with the increase in temperature. A higher temperature is beneficial to dislocation activation, resulting in increased plastic deformation, reduced work-hardening capacity and a lower strength.
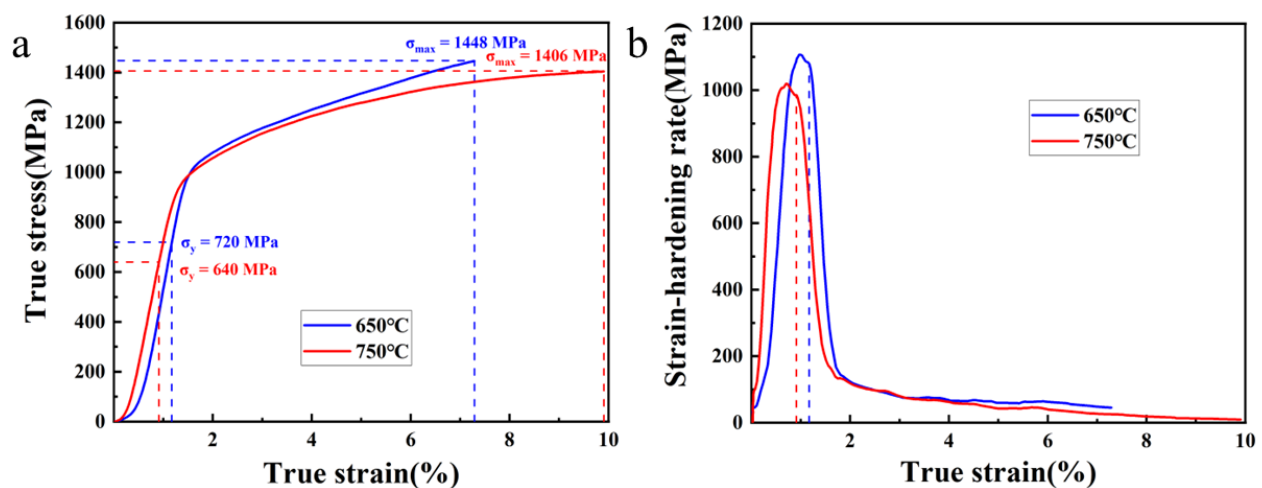


**Figure 1.** (**a**) Compression true stress-true strain curve of FGH96 at 650 °C and 750 °C. (**b**) Strain-hardening rate curve of FGH96 at 650 °C and 750 °C.

The two-dimensional XRD measurements taken after the compression at 650 °C and 750 °C are shown in Figure 2a,b, respectively. It can be seen that no detectable phase transition occurred during the compression process. The diffraction peaks before and after deformation were both composed of $\gamma'$ phase characteristic peaks and $\gamma/\gamma'$ mixed peaks. After compression, the reflections of (111), (200), (220), (311) and (222) were enhanced. The scattered points became more continuous, which was related to the increase in dislocation

density and the formation of low-angle grain boundaries during plastic deformation [18]. The LD was subjected to large compressive stress, resulting in lattice distortion and a diffraction angle deviation to the right. Under the influence of the Poisson effect, the TD was subjected to tensile stress, and thus the diffraction angle shifted to the left, resulting in bending along the azimuth direction of the diffraction ring. Textures were formed after compression at 750 °C. The reflection intensity distributions in (111), (200), (311) and $(222)_{\gamma'}$ were similar. Reflections at $\varphi = \sim 35°$, $\varphi = \sim 90°$ and $\varphi = \sim 145°$ had a higher intensity, while the reflection of the $(220)_{\gamma'}$ was stronger at $\varphi = \sim 0°$, $\varphi = \sim 60°$, $\varphi = \sim 120°$ and $\varphi = \sim 180°$. This was caused by grain rotation to favorable orientations during plastic deformation [19].
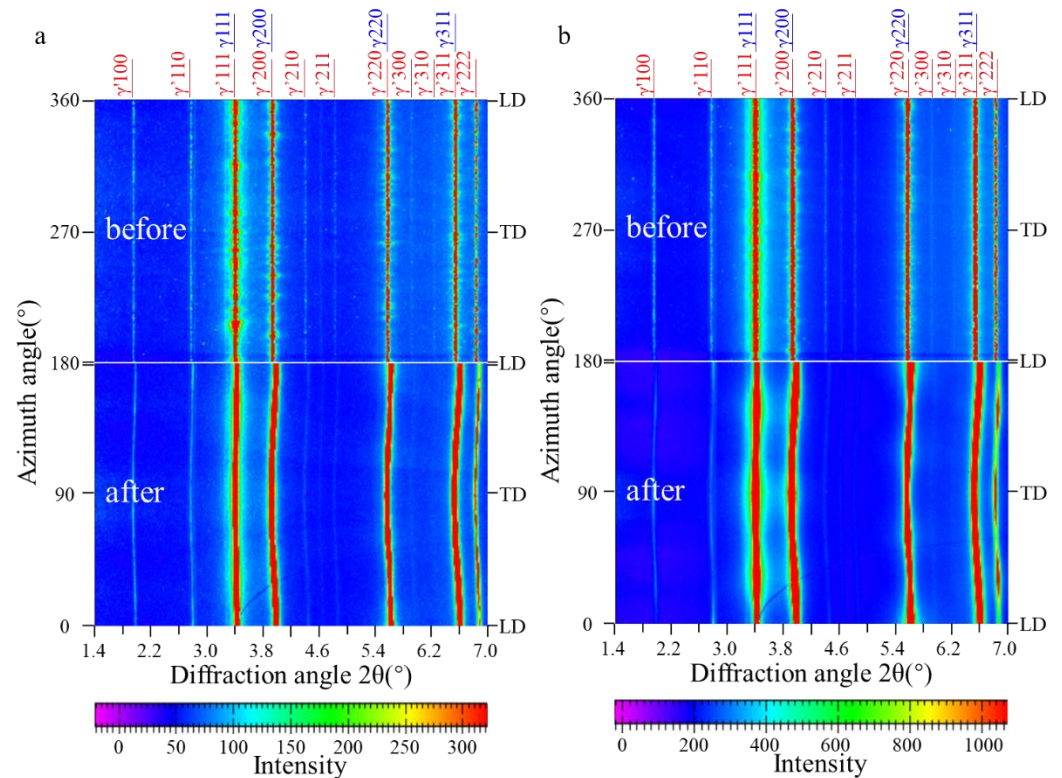


**Figure 2.** Unrolled two-dimensional diffraction rings of the sample before and after compression at (**a**) 650 °C and (**b**) 750 °C.

Figure 3a shows the evolution diagram of true stress-lattice strain of the FGH96 sample at 750 °C. In order to eliminate the complex influence of the Poisson effect on the lattice strain perpendicular to the LD (i.e., the TD), the change in the lattice strain parallel to the LD is specifically discussed. Since the lattice strain in the LD was negative, an absolute value was used for discussion in this paper. In the elastic deformation stage, each lattice plane presented an elastic response. The evolution of lattice strain was determined by the elastic anisotropy. The maximum stiffness was found in the <111> direction, while the minimum stiffness was found in the <200> direction, consistent with other studies [20–22]. In the elasto–plastic transition stage, when the stress reached 640 MPa, the slope of the (200) curve gradually decreased, and the load became larger. In the vicinity of 900 MPa, upward migration appeared in the (111) curve initially, and then plastic deformation occurred. Until the stress further increased to 1000 MPa, the $\gamma/\gamma'$ mixed peaks of (200), (220) and (311) yielded and then entered the stable plastic deformation stage. However, the slope of the (111) curve increased rapidly after the downward migration, which involved the loading transfer between grains of different orientations due to plastic anisotropy. In addition, consistent with previous study [20], the (311) curve showed limited lattice strain and a small deviation. After unloading, the (200) lattice plane had the maximum residual lattice strain of 0.47%, while the (111) lattice plane had the minimum residual lattice strain of

0.09%. The true stress-lattice strain curves of the $\gamma$ and $\gamma'$ phases under compression at 750 °C were obtained through peak fitting, as shown in Figure 3b. The simultaneous change of the (220) lattice plane below 1100 MPa indicated that the $\gamma$ and $\gamma'$ had a similar elastic modulus. Subsequently, the $\gamma$ phase first yielded, and then plastic deformation occurred, while the $\gamma'$ phase remained elastic. However, in the elastic deformation stage, the $<200>_\gamma$ direction bore more load than the $\gamma'$. In the elasto–plastic deformation stage, after around 1000 MPa, the load partitioning of the $\gamma$ and $\gamma'$ phases changed. The $(200)_\gamma$ began to shift upwards and plastic deformation occurred, while the $(200)_{\gamma'}$ was still in the elastic stage, indicating that the stress was transferred from the yielded $\gamma$ phase to the $\gamma'$ phase. When the stress reached around 1100 MPa, the $(220)_\gamma$ began to show plastic deformation, and the curve shifted upward. On the contrary, the $(220)_{\gamma'}$ had greater stress partitioning and still maintained elastic deformation.
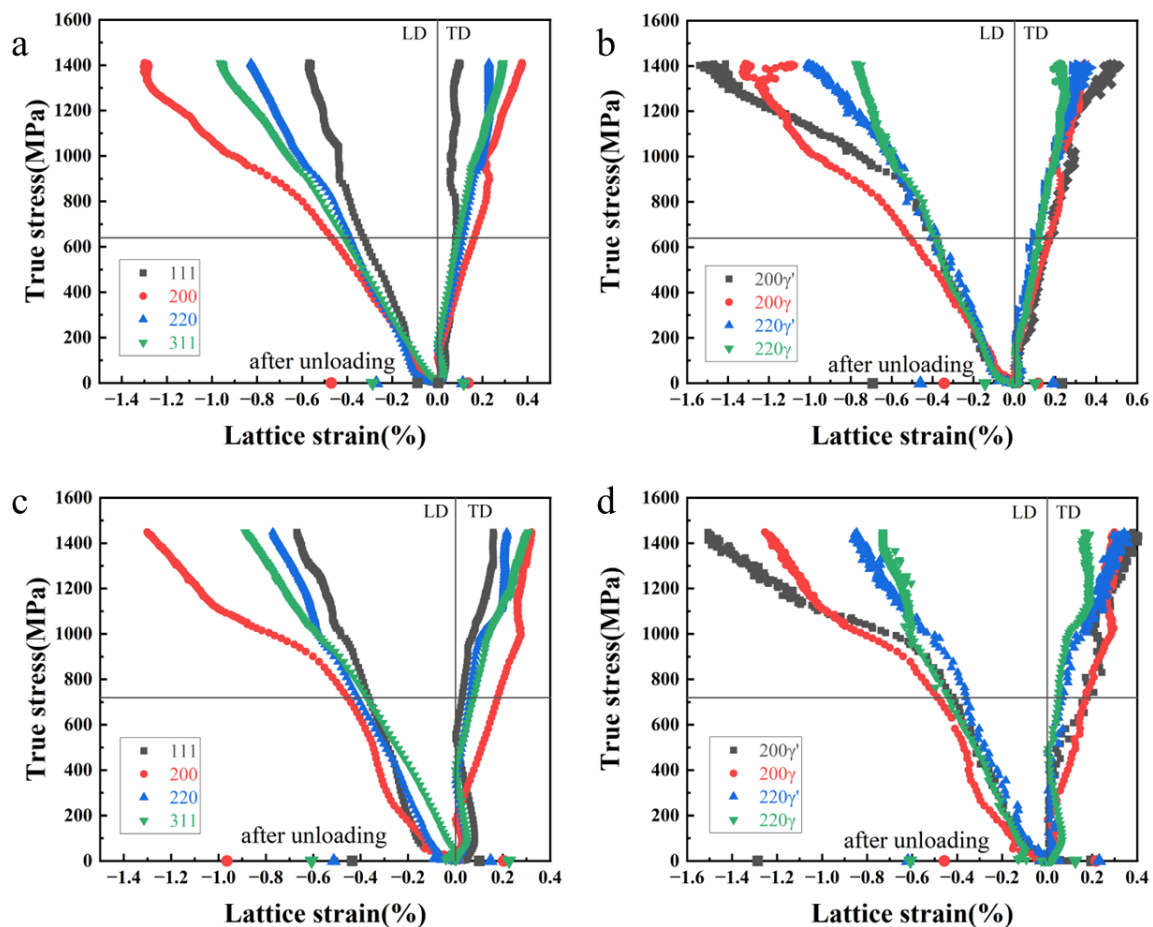


**Figure 3.** Evolution of true stress-lattice strain curves: (**a**) lattice planes of mixed $\gamma/\gamma'$ phases at 750 °C; (**b**) (200) and (220) planes of $\gamma$ and $\gamma'$ phases at 750 °C; (**c**) lattice planes of mixed $\gamma/\gamma'$ phases at 650 °C; and (**d**) (200) and (220) planes of $\gamma$ and $\gamma'$ phases at 650 °C.

Figure 3c shows the evolution of lattice strain during compression at 650 °C. In the elastic deformation stage, each lattice plane basically maintained the elastic response. It should be noted that the asymmetry of the (200) diffraction peak was noticeable. After 720 MPa, the lattice strain of the (200) rose rapidly and bore greater stress. When the stress exceeded 1000 MPa, the true stress-lattice strain curves of all of the lattice planes shifted upward, and obvious plastic deformation occurred simultaneously. According to the residual strain value after unloading (labelled at the abscissa), the residual strain after unloading at 650 °C was greater than that after unloading at 750 °C, which indicated that more internal stress was accumulated during compression at 650 °C. This was consistent with the higher work hardening rate shown in Figure 1, indicating a higher dislocation

density in the microscopic structure. The trend of the residual lattice strain on each lattice plane at 650 °C was consistent with that of 750 °C. The (200) lattice plane had the maximum residual lattice strain, while the (100) had the minimum, which were 0.96% and 0.44%, respectively. From the perspective of the $\gamma$ and $\gamma'$ phase (Figure 3d), consistent with that observed at 750 °C, the elastic modulus of the $(200)_{\gamma'}$, $(220)_{\gamma'}$ and $(220)_{\gamma}$ were similar at 650 °C, whereas the elastic modulus of the $(200)_{\gamma}$ was slightly smaller. After approximately 1050 MPa, the curve of the $(200)_{\gamma}$ shifted upwards and the load was transferred to the $(200)_{\gamma'}$. Afterwards, the $(200)_{\gamma/\gamma'}$ yielded at around 1130 MPa. The $(220)_{\gamma}$ yielded at around 950 Mpa; simultaneously, the $(220)_{\gamma'}$ bore a greater load. Plastic deformation occurred in the $(220)_{\gamma'}$ after 1150 MPa. After unloading at 650 °C, the residual lattice strain of the $(200)_{\gamma'}$ was the highest (around 1.29%), which was still higher than the maximum residual lattice strain of the $(200)_{\gamma'}$ at 750 °C (around 0.69%). It can be seen that the plastic deformation of the $\gamma'$ phase at 650 °C was larger than that at 750 °C, and thus a larger residual lattice strain was accumulated, which was probably caused by the large number of dislocations tangling around the $\gamma'$ particles.

Figure 4 was obtained by deriving the true stress-lattice strain curve, corresponding to the work hardening rates of (111), (200), (220) and (311) lattice plane at 750 °C and 650 °C, respectively. The evolution pattern of lattice strain was almost identical at 750 °C and 650 °C. The main difference was that the lattice strain gradient at 650 °C was more negative. That is, the blue dot in Figure 4 was more distant from zero, which means that the pile-up rate of dislocation at the $\gamma'$ interface at 650 °C was greater than that at 750 °C, consistent with the macro stress–strain curve shown in Figure 1. The discontinuous change in the curve indicated that dynamic recovery was initiated simultaneously in the microstructure. However, the overall trend of the curve indicated that work hardening was still dominant.
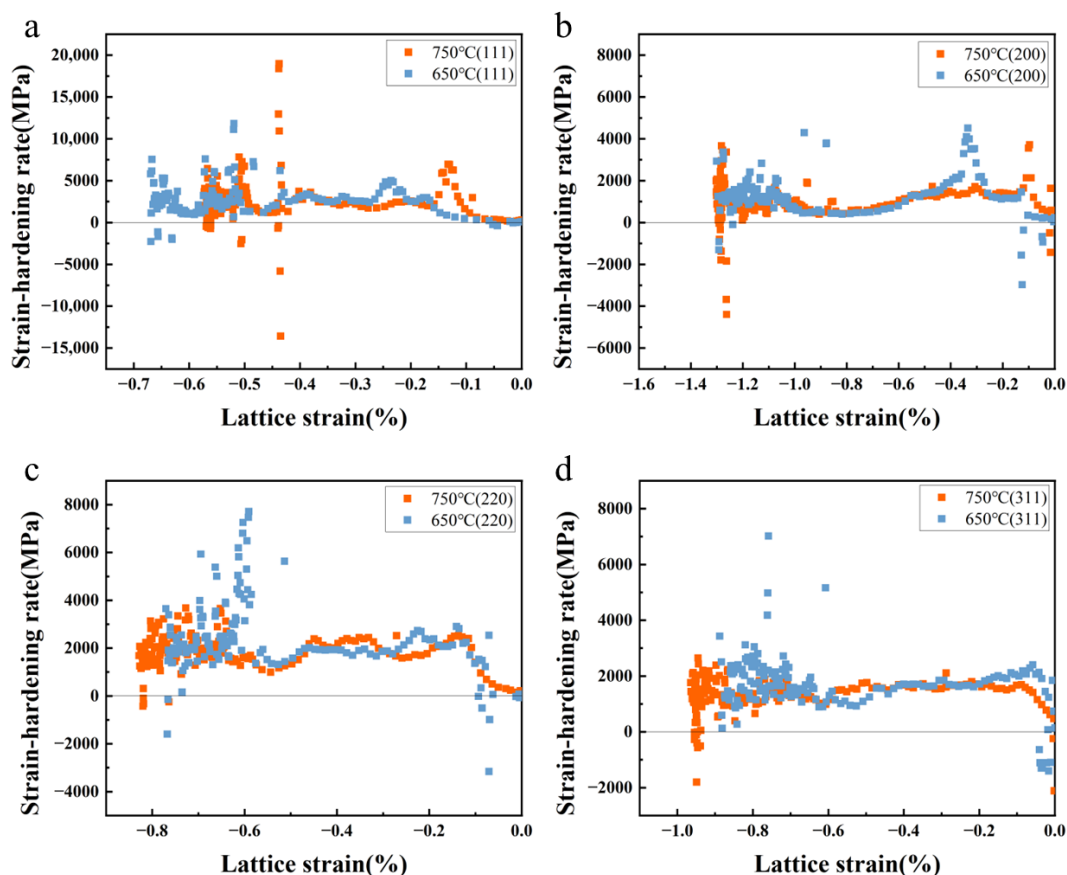


**Figure 4.** Work hardening rates of true stress-lattice strain curve: (**a**) (111); (**b**) (200); (**c**) (220); (**d**) (311).

The microstructures of the original and compressed samples were observed using TEM, and the results are shown in Figure 5. As can be seen from Figure 5a, it is reasonable that almost no dislocations existed in the sample before compression, because the sample was annealed for 16 h, which made the $\gamma'$ phase reach a relatively stable morphology. After the compression at 650 °C, the dislocations multiplicated substantially, which were mainly tangled around the $\gamma'$ particles and severely blocked (Figure 5b), indicating that the $\gamma'$ phase was subjected to strong stress concentrations. Due to the ordered structure of $\gamma'$ phase, the critical shear stress of the dislocation activation was high, which made it difficult for the dislocations to slip into the interior of the $\gamma'$ phase, resulting in dislocation pile-up at the interface of $\gamma/\gamma'$. After slipping for a certain distance in the $\gamma$ phase, the dislocations were quickly blocked by the densely distributed $\gamma'$ phase, and thus the sample showed a strong work hardening effect. During compression at 750 °C (Figure 5c), it can be seen that the density of the dislocation was still high. As the true strain value of the two samples were not identical (limited by the maximum pressure and strength of the indenter), it was difficult to compare the density of dislocation in parallel for the two samples after compression. However, the common feature was that the dislocations were obviously blocked by the $\gamma/\gamma'$ interface. Due to the relatively small amount of plastic deformation of the $\gamma'$ phase at 750 °C, only a few dislocations could slip into the $\gamma'$ phase. This also indicated that the stress concentration was lower than that at 650 °C, which corresponded to the low residual lattice strain in Figure 3.
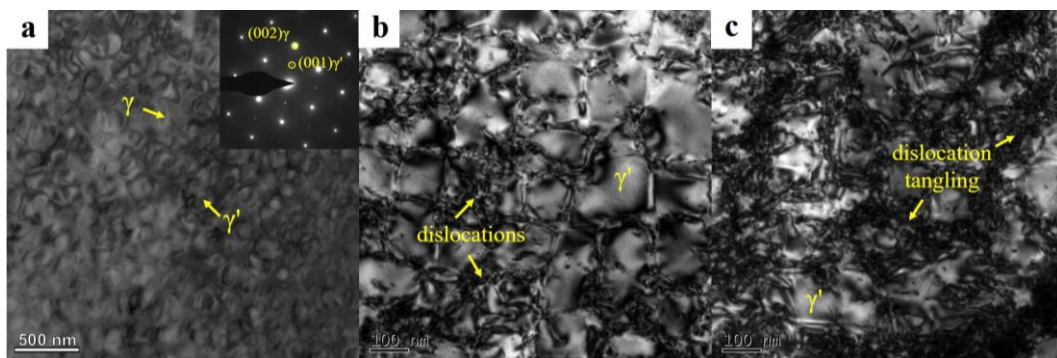


**Figure 5.** TEM observation on the aged and deformed samples: (**a**) aged sample; (**b**) sample deformed to a strain of 7.3% at 650 °C; (**c**) sample deformed to a strain of 9.9% at 750 °C.

## 4. Conclusions

The compression process of nickel-based superalloys with a $\gamma'$ phase volume fraction of 40% at 750 °C and 650 °C was studied using an in situ synchrotron radiation high-energy XRD. In general, the deformation mechanism was basically the same. The $\gamma$ phase deformed prior to the $\gamma'$ phase, and underwent greater plastic deformation. The load was transferred from the $\gamma$ phase to the $\gamma'$ phase. At 650 °C, the $\gamma'$ phase experienced greater plastic deformation, while at 750 °C, the $\gamma'$ particles basically maintained elastic deformation, with a tiny amount of plastic deformation. After unloading at 650 °C and 750 °C, the maximum residual lattice strain of $(200)_{\gamma'}$ was about 1.29% and 0.69%, respectively. At 650 °C, the $(200)_\gamma$ and $(220)_\gamma$ yielded at around 1050 MPa and 950 Mpa, respectively. Additionally, at 750 °C, the $(200)_\gamma$ and $(220)_\gamma$ yielded at about 1000 MPa and 1100 Mpa, respectively. A TEM analysis of the deformed samples was consistent with the evolution of the lattice strain.

**Author Contributions:** Experiments, Data curation, Writing—original draft, H.W.; Conceptualization, Writing—Reviewing and Editing, R.T.; TEM related work, H.S.; Review, A.S.; Preparation of superalloy specimens, G.L.; Review and editing, L.S.; Supervision, T.Z. All authors have read and agreed to the published version of the manuscript.

**Conflicts of Interest:** The authors declare no conflict of interest.

# References

1. Reed, R.C. The physical metallurgy of nickel and its alloys. In *Superalloys-Fundamentals and Applications*; Cambridge University Press: Cambridge, UK, 2006; pp. 33–120.
2. Goodfellow, A.J. Strengthening mechanisms in polycrystalline nickel-based superalloys. *Mater. Sci. Technol.* **2018**, *34*, 1793–1808. [CrossRef]
3. Kozar, R.W.; Suzuki, A.; Milligan, W.W.; Schirra, J.J.; Savage, M.F.; Pollock, T.M. Strengthening mechanisms in polycrystalline multimodal nickel-base superalloys. *Metall. Mater. Trans. A* **2009**, *40*, 1588–1603. [CrossRef]
4. Gai, Y.; Zhang, R.; Yang, J.; Cui, C.; Qu, J. Effects of heat treatment on $\gamma'$ precipitates and tensile properties of a Ni-base superalloy. *Mater. Sci. Eng. A* **2022**, *842*, 143079. [CrossRef]
5. Mukherjee, S.; Sivaprasad, S.; Tarafder, S.; Bhattacharyya, D.; Kar, S.K. Influence of ageing on high temperature tensile deformation of a Ni-based superalloy, HAYNES 282. *J. Alloys Compd.* **2022**, *917*, 165430. [CrossRef]
6. Dong, H.; Xu, T.; Ning, T.; Liu, M.; Wu, D.; Ma, H.; Feng, Z.; Narayanaswamy, B.; Su, R.; Wang, T. Atomic simulations on the deformation mechanisms in nano-crystalline Ni-Al series Ni-based superalloy based on grain size, strain rate and temperature. *J. Mater. Res. Technol.* **2023**, *23*, 77–89. [CrossRef]
7. Xu, Z.; Li, G.; Zhou, Y.; Guo, C.; Huang, Y.; Hu, X.; Li, X.; Zhu, Q. Tension-compression asymmetry of nickel-based superalloys: A focused review. *J. Alloys Compd.* **2023**, *946*, 169313. [CrossRef]
8. Tan, Z.H.; Wang, X.G.; Du, Y.L.; Duan, T.F.; Yang, Y.H.; Liu, J.L.; Liu, J.D.; Yang, L.; Li, J.G.; Zhou, Y.Z.; et al. Temperature dependence on tensile deformation mechanisms in a novel Nickel-based single crystal superalloy. *Mater. Sci. Eng. A* **2020**, *776*, 138997. [CrossRef]
9. Sajjadi, S.A.; Nategh, S.; Isac, M.; Zebarjad, S.M. Tensile deformation mechanisms at different temperatures in the Ni-base superalloy GTD-111. *J. Mater. Process. Technol.* **2004**, *155*, 1900–1904. [CrossRef]
10. Thornton, P.H. Cross slip in phases having the $L1_2$ structure. *Metall. Mater. Trans. B* **1972**, *3*, 291–300. [CrossRef]
11. Kim, I.S.; Choi, B.G.; Hong, H.U.; Yoo, Y.S.; Jo, C.Y. Anomalous deformation behavior and twin formation of Ni-base superalloys at the intermediate temperatures. *Mater. Sci. Eng. A* **2011**, *528*, 7149–7155. [CrossRef]
12. Zhang, P.; Yuan, Y.; Yin, H.; Gu, Y.; Wang, J.; Yang, M.; Yang, G.; Song, X. Tensile properties and deformation mechanisms of Haynes 282 at various temperatures. *Metall. Mater. Trans. A* **2018**, *49*, 1571–1578. [CrossRef]
13. Jaladurgam, N.R.; Kabra, S.; Colliander, M.H. Macro-and micro-mechanical behaviour of a $\gamma'$ strengthened Ni-based superalloy at cryogenic temperatures. *Mater. Des.* **2021**, *209*, 109954. [CrossRef]
14. Jaladurgam, N.R.; Li, H.; Kelleher, J.; Persson, C.; Steuwer, A.; Colliander, M.H. Microstructure-dependent deformation behaviour of a low $\gamma'$ volume fraction Ni-base superalloy studied by in-situ neutron diffraction. *Acta Mater.* **2020**, *183*, 182–195. [CrossRef]
15. Grant, B.M.; Francis, E.M.; Da Fonseca, J.Q.; Daymond, M.R.; Preuss, M. Deformation behaviour of an advanced nickel-based superalloy studied by neutron diffraction and electron microscopy. *Acta Mater.* **2012**, *60*, 6829–6841. [CrossRef]
16. Francis, E.M.; Grant, B.M.; Da Fonseca, J.Q.; Phillips, P.J.; Mills, M.J.; Daymond, M.R.; Preuss, M. High-temperature deformation mechanisms in a polycrystalline nickel-base superalloy studied by neutron diffraction and electron microscopy. *Acta Mater.* **2014**, *74*, 18–29. [CrossRef]
17. Hou, K.; Wang, M.; Zhao, P.; Ou, M.; Li, H.; Ma, Y.; Liu, K. Temperature-dependent yield strength and deformation mechanism of a casting Ni-based superalloy containing low volume-fraction $\gamma'$ phase. *J. Alloys Compd.* **2022**, *905*, 164187. [CrossRef]
18. Liss, K.D.; Yan, K. Thermo-mechanical processing in a synchrotron beam. *Mater. Sci. Eng. A* **2010**, *528*, 11–27. [CrossRef]
19. Yan, K.; Liss, K.D.; Garbe, U.; Daniels, J.; Kirstein, O.; Li, H.; Dippenaar, R. From single grains to texture. *Adv. Eng. Mater.* **2009**, *11*, 771–773. [CrossRef]
20. Goodfellow, A.J.; Kelleher, J.; Jones, N.G.; Dye, D.; Hardy, M.C.; Stone, H.J. The effect of Mo on load partitioning and microstrain evolution during compression of a series of polycrystalline Ni-Based superalloys. *Acta Mater.* **2019**, *176*, 318–329. [CrossRef]
21. Coakley, J.; Dye, D. Lattice strain evolution in a high volume fraction polycrystal nickel superalloy. *Scr. Mater.* **2012**, *67*, 435–438. [CrossRef]
22. Ma, S.; Rangaswamy, P.; Majumdar, B.S. Microstress evolution during in situ loading of a superalloy containing high volume fraction of c0 phase. *Scr. Mater.* **2003**, *48*, 525–530. [CrossRef]